Received: 10 October 2019 | Revised: 3 February 2020 | Accepted: 9 March 2020

DOI: 10.4218/etrij.2019-0465

ORIGINAL ARTICLE

ETRI Journal WILEY

Transversal wideband bandpass filter with a wide stopband and multiple transmission zeros

Li-Tian Wang[1] | **Yang Xiong**[1,2] | **Zhi-Peng Wang**[1] | **Li Gong**[1]

[1]College of Electronic Information and Optical Engineering, Nankai University, Tianjin, China

[2]Southwest China Institute of Electronic Technology, Chengdu, China

Correspondence
Yang Xiong, Southwest China Institute of Electronic Technology, Chengdu, China.
Email: xiongyang0291@163.com

[Correction added on 28 October 2020, after first Online publication: Four authors have been removed from the author list.]

Funding information
Nankai University; National Natural Science Foundation of China, Grant/Award Number: 61101018, 51002081, 61171028.

Herein, we present a compact transversal bandpass filter (BPF) with an extremely wide upper stopband and multiple transmission zeros (TZ). Three signal transmission paths with shorted stubs and open-coupled lines allow signal transmission from input port to output port. Two resonant modes can be excited simultaneously and managed easily for bandpass response. Eleven TZs are achieved via transmission path cancelation; an extremely wide upper stopband with an attenuation level better than –12 dB is achieved up to 11.7 f_0, where f_0 is the center frequency (CF). In addition, bandwidth and CF can be controlled by adjusting electrical lengths. For proof of concept, a wideband BPF centered at 1.04 GHz with 3 dB fractional bandwidths of 49.2% was designed, fabricated, and evaluated. The overall circuit measures $0.045\lambda_g \times 0.117\lambda_g$; good agreement was observed between the measured and simulated results.

KEYWORDS
extremely wide stopband, multi-transmission zeros, transversal signal interference, Wideband BPF

1 | INTRODUCTION

A compact wideband bandpass filter (BPF) with multiple transmission zeros and wide out-of-band suppression free of spurious resonance is in high demand for modern wireless communication systems. Because of their perfect integration capabilities, microstrip BPFs have been studied and developed extensively. However, they generally suffer from spurious harmonic responses, due to the periodic characteristic of transmission lines. Over the past few decades, various approaches and structures have been proposed to overcome this issue using a high-performance BPF that can suppress harmonics without spurious resonance.

BPFs with a broad stopband were achieved by cascading an additional bandstop filter or low pass filter [1,2]. However, with this approach, both circuit size and insertion loss are large. By employing an additional defected grounded structure (DGS), a coupled-line BPF with extended stopband performance was realized [3]. Interdigital capacitance structures were applied to suppress harmonics and wide stopband BPFs without notch-like characteristics [4]. Another conventional attempt employed a stepped-impedance resonator (SIR) to push harmonics to higher frequencies. By properly adjusting the characteristic impedance ratio, wideband BPFs using quarter-/half-wavelength SIRs were demonstrated with suppressed second- and third-harmonic frequencies [5,6]. To obtain BPFs with broad stopband attenuation, transmission zeros (TZs) are frequently introduced to suppress harmonics. Using multimode stub-loaded resonators (MMSLR), wide harmonics-suppressed BPFs with multiple TZs have been achieved [7–9]. Coupled lines also can be applied to construct wideband BPFs with multiple transmission poles (TPs) and TZs [10–13], which broadens the upper stopband.

Recently, transversal signal cancelation techniques have been used to produce multiple TZs, high selectivity, and harmonic suppression [14]. Thus, the design of transversal BPFs has attracted much attention [15–20]. Two transmission paths from input port to output port were designed and transversal signal interaction (TSI) BPF with high selectivity and harmonic suppression was achieved. Unfortunately, few transversal BPFs have more than two transmission paths and previous attempts have rarely obtained wideband BPFs with wide harmonic suppression without spur-like responses.

In this paper, we present a compact wideband BPF with a wide upper stopband based on transversal signal interaction concepts. The transversal BPF consists of three transmission paths from input port to output port. By deriving the transmission matrix of the presented BPF, design specifications are achieved by adjusting the electrical lengths appropriately. Multiple TZs are excited by a multi-transmission path interaction in order to achieve sharp skirt selectivity; the ultra-wide upper stopband is excited up to a dozen times the center frequency (CF). To verify theoretical predictions and demonstrate proof of concept, a compact BPF with 1.04 GHz of CF was designed, fabricated, and evaluated. Measured and simulated results are in good agreement.

2 | DESIGN OF WIDEBAND TSI BPF

The physical layout of the proposed wideband BPF is shown in Figure 1. The proposed transversal wideband BPF comprises a shorted T-shaped structure with corresponding physical lengths and widths denoted by L_1, L_2 and W_1, W_2, respectively; a pair of symmetrical shorted stub-loaded resonators (denoted by L_3, W_3) with parallel coupled lines (labeled L_4, W_4); and an anti-coupled line structure (denoted L_5, W_5 and L_6, W_6). Figure 2 illustrates the ideal transmission line model (TLM) of the BPF. Y_n (n = 1, 2, 3, and 5) and θ_n (n = 1, 2, 3, 4, and 6) represent the characteristic admittances and electrical lengths of counterpart microstrip line, respectively. As can be observed in Figure 2, three transmission paths are adopted to conduct the TSI wideband BPF. The design methodology is demonstrated using an **ABCD** matrix.

As shown in Figure 2, the **ABCD** matrix of an open parallel coupled line and microstrip line can be respectively defined as [21]:

$$M_{\mathrm{PCL}} = \begin{bmatrix} \dfrac{Z_{\mathrm{oe}}+Z_{\mathrm{oo}}}{Z_{\mathrm{oe}}-Z_{\mathrm{oo}}} & j\dfrac{-2jZ_{\mathrm{oe}}Z_{\mathrm{oo}}\cot\theta_4}{Z_{\mathrm{oe}}-Z_{\mathrm{oo}}} \\ \dfrac{2j\tan\theta_4}{Z_{\mathrm{oe}}-Z_{\mathrm{oo}}} & \dfrac{Z_{\mathrm{oe}}+Z_{\mathrm{oo}}}{Z_{\mathrm{oe}}-Z_{\mathrm{oo}}} \end{bmatrix} \tag{1}$$

$$M_{L3} = \begin{bmatrix} \cos\theta_3 & j\sin\theta_3/Y_3 \\ j\sin\theta_3 Y_3 & \cos\theta_3 \end{bmatrix}. \tag{2}$$

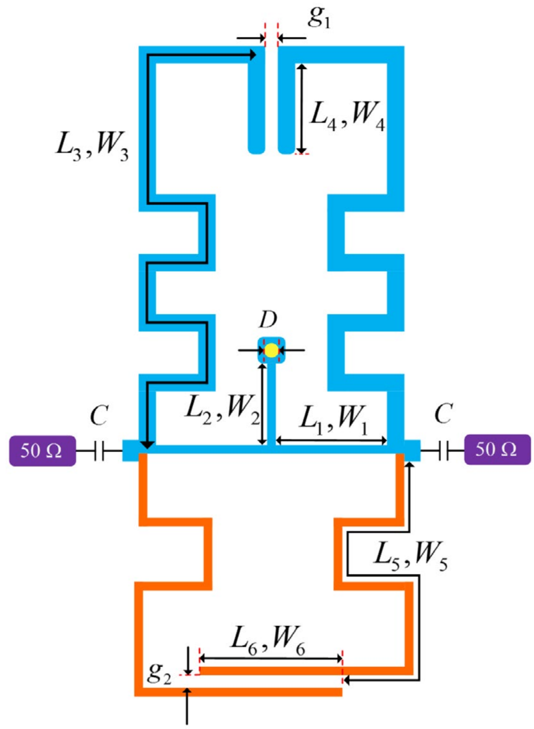

FIGURE 1 Geometrical configuration of the proposed TSI wideband BPF

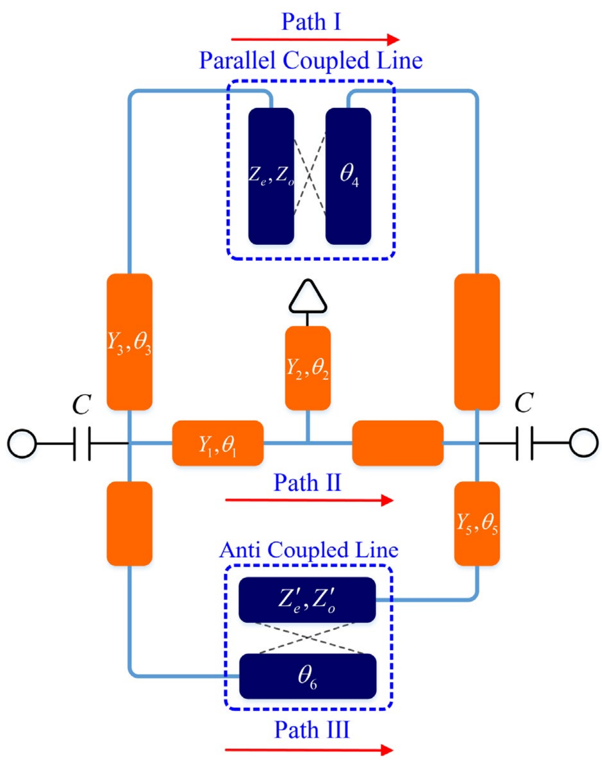

FIGURE 2 An ideal TLM model of the proposed BPF

It follows that the **ABCD** matrix of path I can be expressed and derived by

$$M_{\mathrm{PathI}} = \begin{bmatrix} A_1 & B_1 \\ C_1 & D_1 \end{bmatrix} = M_{L3} \times M_{\mathrm{PCL}} \times M_{L3} \tag{3}$$

where

$$A_1 = \cos\theta_3 \frac{Z_{oe}+Z_{oo}}{Z_{oe}-Z_{oo}} + \frac{2\sin\theta_3\cos\theta_3\tan\theta_4}{(Z_{oe}-Z_{oo})Y_3} + \frac{2Z_{oe}Z_{oo}\cot\theta_4\sin\theta_3\cos\theta_3 Y_3}{Z_{oe}-Z_{oo}} - \frac{\sin^2\theta_3(Z_{oe}+Z_{oo})}{Z_{oe}-Z_{oo}}, \tag{4}$$

$$B_1 = j\sin\theta_3\cos\theta_3 \frac{Z_{oe}+Z_{oo}}{(Z_{oe}-Z_{oo})Y_3} - \frac{2j\sin^2\theta_3\tan\theta_4}{(Z_{oe}-Z_{oo})Y_3^2} - \frac{2jZ_{oe}Z_{oo}\cos\theta_4\cos^2\theta_3}{(Z_{oe}-Z_{oo})} + \frac{j\sin\theta_3\cos\theta_3(Z_{oe}+Z_{oo})}{Y_3}, \tag{5}$$

$$C_1 = \frac{j\sin\theta_3\cos\theta_3 Y_3(Z_{oe}+Z_{oo})}{Z_{oe}-Z_{oo}} + \frac{2j\tan\theta_4\cos^2\theta_3}{Z_{oo}-Z_{oe}} \times \frac{2jZ_{oe}Z_{oo}\sin^2\theta_3\cot\theta_4}{Z_{oe}-Z_{oo}} - \frac{j\sin\theta_3\cos\theta_3 Y_3(Z_{oe}+Z_{oo})}{Z_{oe}-Z_{oo}}, \tag{6}$$

$$D_1 = -\frac{\sin^2\theta_3(Z_{oe}+Z_{oo})}{Z_{oe}-Z_{oo}} - \frac{2\tan\theta_4\cos\theta_3\sin\theta_3}{(Z_{oe}-Z_{oo})Y_3} + \frac{2Z_{oe}Z_{oo}\sin\theta_3\cot\theta_4\cos\theta_3}{(Z_{oe}-Z_{oo})Y_3} + \frac{\cos^2\theta_3(Z_{oe}+Z_{oo})}{Z_{oe}-Z_{oo}}. \tag{7}$$

For transmission path II, the shorted stub-loaded T-shape resonator, the **ABCD** matrix can be obtained as follows

$$M_{\text{PathII}} = \begin{bmatrix} A_2 & B_2 \\ C_2 & D_2 \end{bmatrix} = M_{L1} \times M_{\text{stub2}} \times M_{L1} \tag{8}$$

where

$$\begin{aligned} A_2 &= \cos^2\theta_1 + Y_2\sin\theta_1\cos\theta_1\tan\theta_2/Y_1 - \sin^2\theta_1, \\ B_2 &= j\frac{\sin\theta_1\cos\theta_1}{Y_1} + \frac{jY_2\sin^2\theta_1\tan\theta_2}{Y_1^2} + j\sin\theta_1\cos\theta_1/Y_1, \\ C_2 &= j\sin\theta_1\cos\theta_1 Y_1 - jY_2\cos^2\theta_1\tan\theta_2 + j\sin\theta_1\cos\theta_1 Y_1, \\ D_2 &= -\sin^2\theta_1 + Y_2\cos\theta_1\tan\theta_2\sin\theta_1/Y_1 + \cos^2\theta_1. \end{aligned} \tag{9}$$

Transmission path III contains an anti-coupled line, for which the **ABCD** matrix can be written as

$$M_{\text{ACL}} = \begin{bmatrix} \frac{Z'_{oe}+Z'_{oo}}{Z'_{oe}-Z'_{oo}}\cos\theta_6 & j\frac{(Z'_{oe}-Z'_{oo})^2-(Z'_{oe}+Z'_{oo})^2\cos^2\theta_6}{2(Z'_{oe}-Z'_{oo})\sin\theta_6} \\ j\frac{2\sin\theta_6}{Z'_{oe}-Z'_{oo}} & \frac{Z'_{oe}+Z'_{oo}}{Z'_{oe}-Z'_{oo}}\cos\theta_6 \end{bmatrix}. \tag{10}$$

Thus, the **ABCD** matrix of transmitting path III can be deduced from

$$M_{\text{PathIII}} = \begin{bmatrix} A_3 & B_3 \\ C_3 & D_3 \end{bmatrix} = M_{L5} \times M_{\text{ACL}} \times M_{L5} \tag{11}$$

where

$$A_3 = \frac{Z'_{oe}+Z'_{oo}}{Z'_{oe}-Z'_{oo}}\cos^2\theta_5\cos\theta_6 - \frac{(Z'_{oe}-Z'_{oo})^2-(Z'_{oe}+Z'_{oo})^2\sin\theta_5\cos\theta_5\cos^2\theta_6 Y_5}{2(Z'_{oe}-Z'_{oo})\sin\theta_6} - \frac{2\sin\theta_5\sin\theta_6\cos\theta_5}{(Z'_{oe}-Z'_{oo})Y_5} - \sin^2\theta_5\cos\theta_6\left(\frac{Z'_{oe}+Z'_{oo}}{Z'_{oe}-Z'_{oo}}\right), \tag{12}$$

$$B_3 = j\frac{Z'_{oe}+Z'_{oo}}{Z'_{oe}-Z'_{oo}}\sin\theta_5\cos\theta_5\cos\theta_6/Y_5 - \frac{2j\sin^2\theta_5\sin\theta_6}{(Z'_{oe}-Z'_{oo})Y_5^2} + j\frac{(Z'_{oe}-Z'_{oo})^2-(Z'_{oe}+Z'_{oo})^2\cos^2\theta_6\cos^2\theta_5}{2(Z_{oe}-Z_{oo})\sin\theta_6} + j\frac{\sin\theta_5\cos\theta_5\cos\theta_6}{Y_5}\left(\frac{Z'_{oe}+Z'_{oo}}{Z'_{oe}-Z'_{oo}}\right), \tag{13}$$

$$C_3 = j\sin\theta_5\cos\theta_5\frac{Z'_{oe}+Z'_{oo}}{Z'_{oe}-Z'_{oo}} + 2j\frac{\sin\theta_6\cos^2\theta_5}{Z'_{oe}-Z'_{oo}} - \frac{(Z'_{oe}-Z'_{oo})^2-(Z'_{oe}+Z'_{oo})^2\cos^2\theta_6\sin^2\theta_5 Y_5^2}{2(Z'_{oe}-Z'_{oo})\sin\theta_6} + \cos^2\theta_5\cos\theta_6\left(\frac{Z'_{oe}+Z'_{oo}}{Z'_{oe}-Z'_{oo}}\right), \tag{14}$$

$$D_4 = -\sin^2\theta_5\cos\theta_6\frac{Z'_{oe}+Z'_{oo}}{Z'_{oe}-Z'_{oo}} - \frac{2\sin\theta_5\cos\theta_5\sin\theta_6}{(Z'_{oe}-Z'_{oo})Y_5} - \frac{(Z'_{oe}-Z'_{oo})^2-(Z'_{oe}+Z'_{oo})^2\cos^2\theta_6\cos\theta_5\sin\theta_5 Y_5}{2(Z'_{oe}-Z'_{oo})\sin\theta_6} + \cos^2\theta_5\cos\theta_6\left(\frac{Z'_{oe}+Z'_{oo}}{Z'_{oe}-Z'_{oo}}\right). \tag{15}$$

After converting from **ABCD**-parameters to the admittance matrix, the **Y**-matrix of the proposed wideband BPF can be defined and calculated from the following equations:

$$Y = Y' + Y'' + Y''' = \begin{bmatrix} Y'_{11}+Y''_{11}+Y'''_{11} & Y'_{12}+Y''_{12}+Y'''_{12} \\ Y'_{21}+Y''_{21}+Y'''_{21} & Y'_{22}+Y''_{22}+Y'''_{22} \end{bmatrix} = \begin{bmatrix} Y_{11} & Y_{12} \\ Y_{21} & Y_{22} \end{bmatrix} \tag{16}$$

where Y', Y'', and Y''' represents the admittance matrices of transmit paths I, II, and III, respectively. Consequently, the transmission coefficient and reflection coefficient can be extracted separately as follows [22]:

$$S_{21} = -\frac{2Y_{21}Y_0}{\Delta Y}, \tag{17}$$

$$S_{11} = \frac{(Y_0-Y_{11})(Y_0+Y_{22})+Y_{12}Y_{21}}{\Delta Y}, \tag{18}$$

where $\Delta Y = (Y_{11}+Y_0)(Y_{22}+Y_0) - Y_{12}Y_{21}$ and Y_0 is 0.02 S. For simplicity, $\theta_1 = \theta_2 = \theta_4 = 10°$, $\theta_3 = \theta_5 = 30°$, and $Y_1 = Y_2 = Y_3 = Y_5 = 0.01$ S are assumed. The reference frequency, f_0, is set as 1.04 GHz to calculate electrical length. The resonant frequencies are solved using (17) and (18) with the numerical calculation method. When $S_{21} = 1$, the transmission poles of the proposed configuration can be derived and two resonant modes can be excited in the neighborhood of the design passband. The influence of the TSI wideband BPF primary electrical lengths on resonant frequencies is shown in Figures 3 and 4, which plot resonant frequencies versus θ_1, θ_2, θ_3, and θ_5. Two resonant modes are indicated by f_1 and f_2. As shown in Figure 3, f_1 decreases with increasing θ_1 or θ_2, while f_2 remains unchanged with variation in θ_2. Both f_1 and f_2 shift down as θ_3 enlarges, whereas θ_5 has a very slight effect on f_1 and f_2, as can be seen in Figure 4. Thus, the two resonant modes can be easily controlled by selecting proper electrical length values. The centered frequency, f_0, and fractional bandwidth, *fbw*, can be estimated in general as below:

$$\begin{cases} BW = f_2 - f_1, \\ f_0 = \dfrac{f_1 + f_2}{2}, \\ fbw = BW/f_0, \end{cases} \tag{19}$$

where *BW* represents the bandwidth of BPF. Therefore, a suitable zone to achieve design specifications (fbw = 50%, $f_0 = 1.04$) can be found readily in Figures 3 and 4. First, $\theta_1 = 6°$, $\theta_2 = 4°$, and $\theta_3 = 40°$ are selected, since θ_1, θ_2, and θ_3 have a major effect on f_1 and f_2. Indeed, the two microstrip lines denoted by (L_1, W_1) and (L_3,W_3) with electrical length $\theta_1 + \theta_3 \approx 45°$ (reference frequency, 1.04 GHz) are 1/4 λ resonator, which serves as the primary physical mechanism for resonance in the proposed TSI BPF.

Transmission zeros versus various θ_5 and θ_6 values are shown in Figures 5 and 6. The generation of transmission zeros is mainly attributed to the cancellation effect of multiple transmission paths from input port to output port. It can be seen in Figures 5 and 6 that resonant modes f_1 and f_2 remain almost unchanged as θ_5 and θ_6 vary. By properly arranging θ_5 and θ_6, 11 TZs and a wide stopband of up to 11.7 f_0 can be realized. Thereafter, the design parameters for the proposed BPF were chosen as $Y_1 = Y_2 = Y_3 = Y_5 = 0.01$ S and $\theta_1 = 6°$, $\theta_2 = 4°$, $\theta_3 = 40°$, $\theta_4 = 8°$, $\theta_5 = 2°$, $\theta_6 = 10°$. $Z_1 = Z_2 = Z_4 = 115\ \Omega$, $Z_3 = 45\ \Omega$, and Z_n (n = 1, 2, 3, and 4) denote the characteristic impedance of each transmission line.

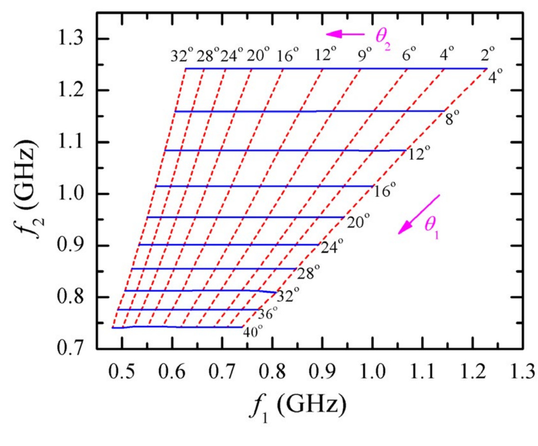

FIGURE 3 Resonant frequencies with varying θ_1 and θ_2

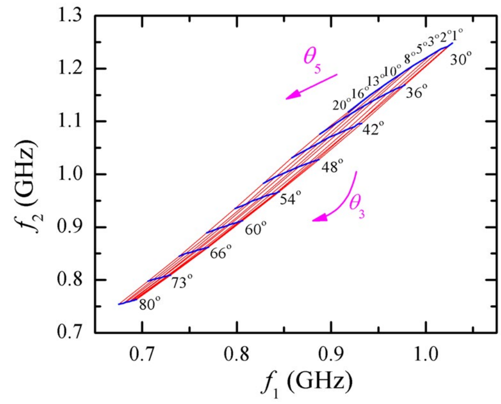

FIGURE 4 Resonant frequencies versus θ_3 and θ_5

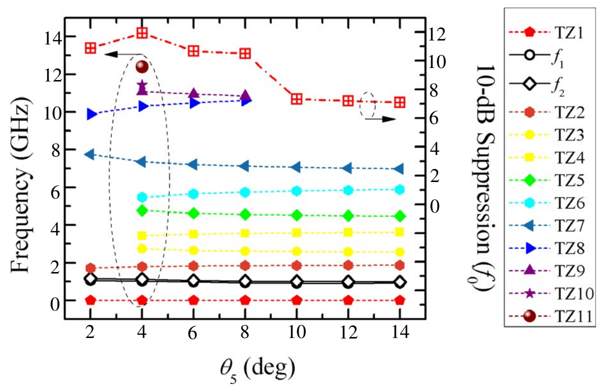

FIGURE 5 Resonant modes and TZs versus θ_5

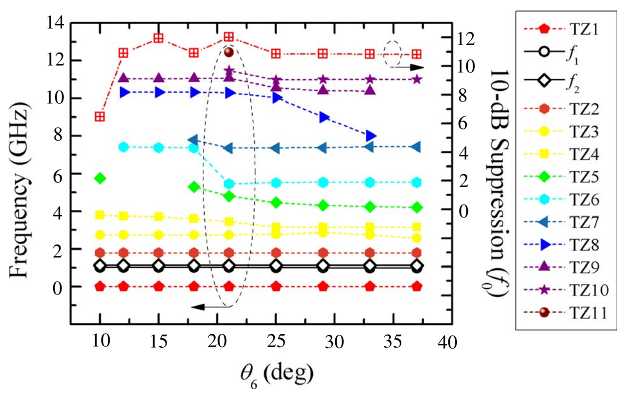

FIGURE 6 Resonant modes and TZs versus θ_6

To assure suitable external coupling strength and desired in-band return loss, the desired external quality value is fulfilled by selecting the proper value of capacitance, C, which can be employed as an admittance inverter. As shown in Figure 7, capacitance has a minor effect on the transmission coefficient, S_{21}, meanwhile changes in the capacitor can effectively manage return loss within the passband. Subsequently, the initial value of lumped capacitor was 2.9 pF.

As demonstrated in Figure 8, the S-parameter responses of the wideband BPF are simulated using the ideal TLM. Two transmission poles form a wideband characteristic. Further, unwanted high-order BPF resonant modes can be suppressed by introducing 12 TZs. To further investigate the physical mechanism to generate TZs, the transmission coefficients, S_{21}, of three configurations are compared in Figure 9. The shorted stub-loaded resonator (without Path III and PCL) retains bandpass characteristics. Current distribution of the proposed configuration at CF is portrayed in Figure 10, which also indicates that Path II is the primary transmission path. The purple short-dashed line in Figure 9 indicates frequency response, which has sharper sidebands and improved out-of-band attenuation (this is shown in blue in Figure 1 as transmission response (Path I + Path II)). With three transmission paths, the proposed wideband BPF yields more transmission zeros; an extremely wide stopband can be realized.

Overall, the mechanism of TZ formation for the transmission characteristic of the shorted stub-loaded resonator is attributed shorting of the transmission signal from port 1 to port 2 when the input impedance of stubs is zero. Compared to the transmission characteristic of the shorted stub-loaded resonator, seven additional TZs can be generated via the TSI scheme, which results in the cancellation of three signals at a certain frequency. Therefore, using TSI concepts, the BPF can achieve wider suppression and higher attenuation of the upper stopband.

Furthermore, the rejection level for out-of-band suppression can be modified. Higher suppression can be achieved

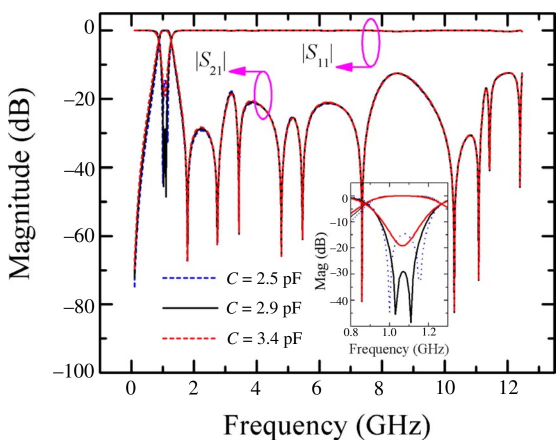

FIGURE 7 Relationship between in-band return loss and varied C

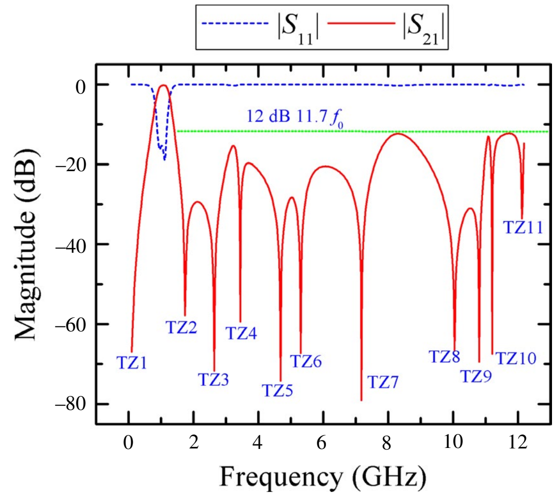

FIGURE 8 Simulated results of proposed BPF with multi-TZs

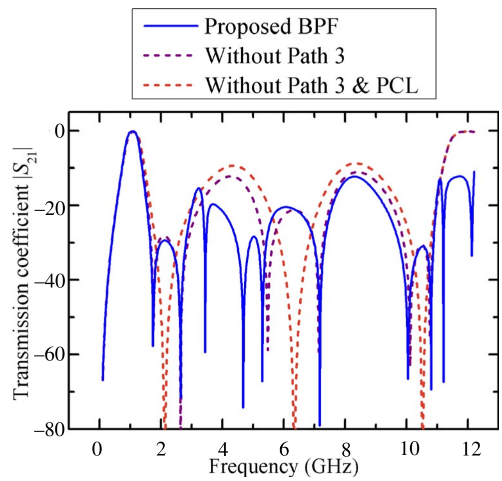

FIGURE 9 Simulated transmission coefficients by configuration

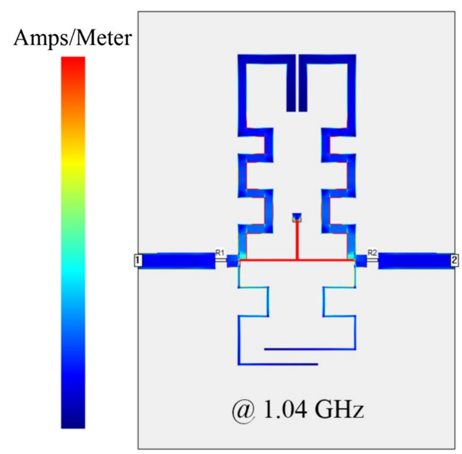

FIGURE 10 Current density distribution of the proposed TSI BPF

by fine-tuning θ_5. Moreover, a wide stopband (up to 7.64 f_0 with attention level of –20 dB) can be obtained at θ_5 of 2°, as sketched in Figure 11.

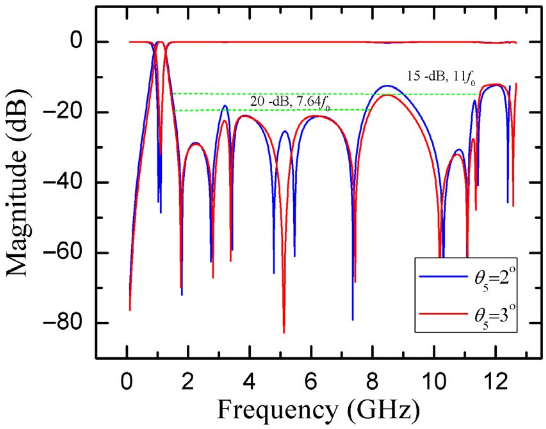

FIGURE 11 Transmission characteristics versus θ_5

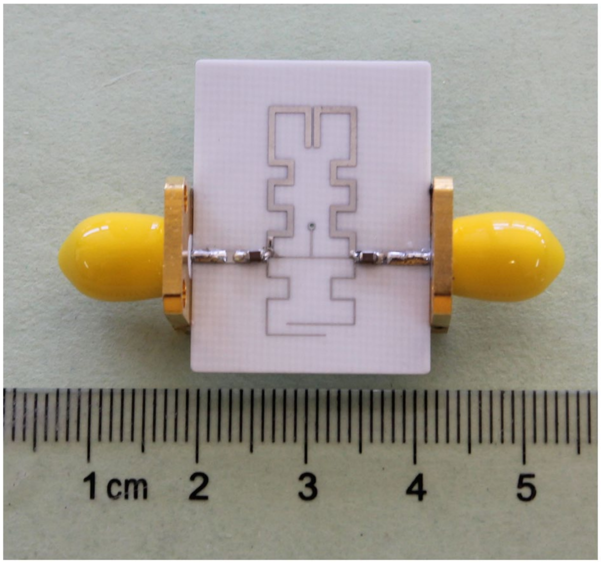

FIGURE 12 Photograph of the implemented transversal wideband BPF

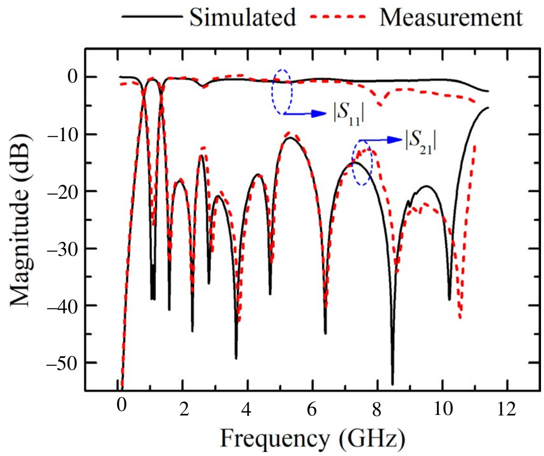

FIGURE 13 Comparison of EM simulated results and measurement results

3 | VALIDATION OF FABRICATION AND MEASUREMENT

A wideband BPF was simulated, fabricated, and evaluated to verify this theoretical approach. A photograph of the fabricated BPF is shown in Figure 12. The proposed filter is fabricated on a substrate of Rogers 4003C with a relative dielectric constant of 3.55, thickness of 0.508 mm, and loss tangent of 0.0027. Using a full-wave electromagnetic (EM) simulator, the physical dimensions of the BPF were optimized as follows: L_1 = 3.825, L_2 = 2.65, L_3 = 24.65, L_4 = 3.875, L_5 = 12.875, L_6 = 3.7; W_1 = 0.125, W_2 = 0.15, W_3 = 0.6, W_4 = 0.6, W_5 = 0.125, W_6 = 0.125; D = 0.3; g_1= = 0.2, g_2 = 0.9 (units: mm). The wideband filter is compact, measuring 8.1 mm × 21.25 mm (excluding feed lines), which corresponds to approximately 0.045 λg × 0.117 λg,

TABLE 1 Performance comparison with previous BPFs

Ref	CF (GHz)	3-dB FBW(%)	TZs	IL (dB)	RL (dB)	Poles	Upper stopband	Circuit Size ($\lambda_g \times \lambda_g$)
[7]	3.2	20.6	6	2.2	12.5	6	2.9 f_0 (–20 dB)	0.61 × 1.06
[8]	3	43.3	4	0.6	17	4	2.5 f_0 (–10 dB)	0.1 × 0.13
[9]	3	87	3	0.6	15.8	4	4.2 f_0 (–19.4 dB)	0.31 × 0.73
[11]	2.05	60	5	0.6	20	5	2.7 f_0 (–10 dB)	0.48 × 0.24
[12]	1.5	10	5	1.28	20	3	1.6 f_0 (–32 dB)	0.27 × 0.22
[13]	2.1	21.9	8	1.52	10	5	3 f_0 (–18 dB)	0.28 × 0.39
[15]	3.05	62	8	1.1	15	4	2.7 f_0 (–20 dB)	0.625 × 0.16
[16]	3	36.3	2	1.4	15	3	2.8 f_0 (–15 dB)	0.39 × 0.19
[18]	2.4/3.7	8/4.6	6	0.3	20	2/2	3.6 f_0 (–10 dB)	0.21 × 0.18
[19]	3	50	6	0.4	15	5	2.75 f_0 (–14 dB)	0.68 × 0.53
This work	1.04	49.2	11	0.12	26.2	2	11 f_0 (–12 dB)/ 7.6 f_0 (–20 dB)	0.045 × 0.117

where λg is the guided wavelength of a 50 Ω microstrip line at 1 GHz.

Measurements were characterized using an Agilent E5071C vector network analyzer. Simulated and measured results are plotted in Figure 13. Measured CF is centered at 1.04 GHz with a –3 dB fractional bandwidth (FBW) of 49.2%. The measured insertion loss (IL) is 0.12 dB at center frequency, and the return loss (RL) is better than 26 dB. Moreover, an ultra-wide upper stopband (up to 11.7 f_0) is achieved with –12 dB attenuation, due to multiple TZs. This work is compared to previously published reports in Table 1; by comparison, the proposed wideband BPF has an extremely wide stopband, multiple TZs, compact size, and low IL.

4 | CONCLUSION

Herein, we present a transversal wideband BPF based on TSI concepts; the BPF was characterized via admittance matrix analysis. Multiple TZs were constructed via multi-transmission path signal cancellation. An extremely wide upper stopband of up to 11.7 f_0 with a suppression level of −12 dB was measured. The designed BPF exhibits many advantages, such as compact size, excellent harmonics suppression, and low IL, indicating its promise for modern RF and wireless communication systems.

ORCID

Li-Tian Wang https://orcid.org/0000-0002-1618-1008

REFERENCES

1. C. W. Tang and M. G. Chen, *A microstrip ultra-wideband bandpass filter with cascaded broadband bandpass and bandstop filters*, IEEE Microw. Wireless Compon. Lett. **55** (2007), no. 11, 2412–2418.
2. K. F. Chang and K. W. Tam, *Miniaturized cross-coupled filter with second and third spurious responses suppression*, IEEE Microw. Wireless Compon. Lett. **15** (2005), no. 2, 122–124.
3. J.-S. Park, J.-S. Yun, and D. Ahn, *A design of the novel coupled-line bandpass filter using defected ground structure with wide stopband performance*, IEEE Microw. Wireless Compon. Lett. **50** (2002), no. 9, 2037–2043.
4. H.-W. Yue et al., *A compact high-temperature superconducting band-pass filter with wide upper stopband*, Phys. C: Superconductivity Its Applicat. **557** (2019), 1–6.
5. H.-Y. Pan, R. Y. Yang, and J.-S. Lin, *Design of a wideband bandpass filter with a high band selectivity and a wide stopband*, J. Electromagnet. Wave. **25** (2011), no. 1, 1863–1873.
6. H. Mohsen, A. Hamid, and H. Akram, *Design of microstrip quasi-elliptic bandpass filter with upper wide stopband using quarter-wavelength stepped-impedance resonators*, J. Electromagnet. Wave. **33** (2013), no. 7, 507–516.
7. W. Feng et al., *Bandpass filter loaded with open stubs using dual-mode ring resonator*, IEEE Microw. Wireless Compon. Lett. **25** (2015), no. 5, 295–297.
8. J.-M. Huang, B. Zhang, and S. S. Li, *Novel compact quad-mode wideband bandpass filter with wide stopband using T-shaped resonator*, J. Electromagnet. Wave. **28** (2014), no. 3, 326–333.
9. Z.-P. Li, T. Su, and C.-H. Liang, *Compact wideband microstrip bandpass filter with wide upper stopband based on coupled-stub loaded resonator*, Int. J. RF. Microw. Comput. Eng. **25** (2014), no. 2, 122–128.
10. K.-D. Xu et al., *Bandpass filter using three pairs of coupled lines with multiple transmission zeros*, IEEE Microw. Wireless Compon. Lett. **28** (2018), no. 7, 2–4.
11. K.-D. Xu, D. Li, and Y. Liu, *High-selectivity wideband bandpass filter using simple coupled lines with multiple transmission poles and zeros*, IEEE Microw. Wireless Compon. Lett. **29** (2019), no. 2, 107–109.
12. S.-C. Lin, *New microstrip cascaded-quadruplet bandpass filter based on connected couplings and short-ended parallel-coupled line*, IEEE Microw. Wireless Compon. Lett. **24** (2014), no. 1, 2–4.
13. K. Tanii and K. Wada, *Wideband bandpass filter composed of dual-path resonators using coupled-line and transmission line with inductive elements*, IEEE Microw. Wireless Compon. Lett. **24** (2014), no. 1, 14–16.
14. W.-J. Feng, W.-Q. Che, and Q. Xue, *Transversal signal interaction: Overview of high-performance wideband bandpass filters*, IEEE Microw. Mag. **15** (2014), no. 2, 84–96.
15. W.-J. Feng and W. Xue, *Transversal wideband bandpass filter using open/shorted coupled lines*, Electron. Lett. **49** (2013), no. 19, 1235–1237.
16. W.-J. Feng et al., *High selectivity wideband bandpass filter based on transversal signal-interaction concepts and T-shaped structure*, IEEE Microw. Wireless Compon. Lett. **22** (2012), no. 11, 562–564.
17. L.-T. Wang et al., *Design of dual-band bandpass filter with multiple transmission zeros using transversal signal interaction concepts*, IEEE Microw. Wireless Compon. Lett. **29** (2019), no. 1, 32–34.
18. Q.-X. Chu and L.-L. Qiu, *Sharp-rejection dual-band bandstop filter based on signal interaction with three paths*, Microw. Opt. Techn. Lett. **57** (2015), no. 3, 657–660.
19. W.-J. Feng et al., *High selectivity fifth-order wideband bandpass filter with multiple transmission zeros based on transversal signal-interaction concepts*, IEEE Trans. Microw. Theory Tech. **61** (2013), no. 1, 89–97.
20. X.-P. Li, Q. Xia, and J.-J. Zeng, *A compact quadruple-mode ultra-wideband bandpass filter with a broad upper stopband based on transversal-signal interaction concepts*, Prog. Electromagn. Res. **69** (2017), 119–125.
21. D. M. Pozar, *Microwave Engineering*, 3rd ed, Wiley, NY, USA, 2003, pp. 341–345.
22. L. Zhu, S. Sun, and R. Li, *Microwave bandpass filters for wideband communications*, Wiley, NJ, USA, 2012, pp. 45–46.

AUTHOR BIOGRAPHIES

Li-Tian Wang was born in Tianjin, China. He is currently working toward his PhD degree at Nankai University, in Tianjin, China. His main research interests include multi-mode microwave filter, microstrip multiplexer, HTS bandpass filter, planar transversal bandpass filter, microwave substrate integrated waveguide filter, and tunable bandpass filters design.

Yang Xiong was born in Huaihua, Hunan province, China, in 1990. He received the PhD degree from Nankai University, Tianjin, China, in 2018. Now, he is a microwave and millimeter-wave circuit engineer with Southwest China Institute of Electronic Technology.

Zhi-Peng Wang was born in Anyang, Henan province, China, in 1996. He received a B.E. degree in electronic and information engineering from Northeast Agricultural University, in Harbin, China, in 2017, and is currently working toward an M.E. degree at Nankai University, in Tianjin, China. His main research interests include the design of microwave tunable filters and high temperature superconducting tunable filters.

Zhao Li was born in Hohhot, Inner Mongolia province, China. She received a BEng degree from Zhengzhou University. She is currently working toward an ME degree at Nankai University, in Tianjin, China. Her main research interest is tunable filters.

Xia-Qing Li received her BE degree in Chang'an University of China, in Xi'an, China, in 2018, and is currently working toward an ME degree in communication and information systems at Nankai University. Her main research interest is microwave differential filters.

Zhe-Long Liang received his BE degree in communication engineering from Nankai University, in Tianjin, China, in 2017, and is currently working toward an ME degree in communication and information systems. His main research interest is microwave balanced filters.

Li Gong was born in Suzhou, Jiangsu province, China. He received a B.E. degree from Suzhou University of Science and Technology, Suzhou, China, in 2016, and he received his M.E. degree at Nankai University, in Tianjin, China. His main research interests are microwave filters and multiplexer design.

Ming He received his M.Eng. and Ph.D. degrees in electrical engineering from Nankai University, in Tianjin, China, in 2002 and 2008, respectively. Since 1997, he has been with the Department of Electronics at Nankai University, in Tianjin, China, where he became a Professor in 2016. From 2004 to 2009, he held several visiting research appointments at Juelich Research Center and Karlsruhe University, Germany. His research interests include applications of high temperature superconductors, the generation and detection of THz signals, and microwave communications.